The Morávka meteorite fall:
4. Meteoroid dynamics and fragmentation in the atmosphere

J. BOROVIČKA[1*] and P. KALENDA[2]

[1]Astronomical Institute of the Academy of Sciences, 25165 Ondrejov, The Czech Republic
[2]CoalExp, Kosmonautu 2, 70030 Ostrava 3, The Czech Republic
[*]Corresponding author. E-mail: borovic@asu.cas.cz

Abstract–Detailed analysis of the fragmentation of the Morávka meteoroid during the atmospheric entry is presented. The analysis is based on the measurement of trajectories and decelerations of fragments seen in a video and at the locations of energetic fragmentation events from seismic data obtained at several stations in the vicinity of the fireball trajectory. About 100 individual fragments are seen on video frames. Significant deceleration of the fireball at heights of ~45 km revealed that the meteoroid had already fragmented into ~10 pieces with masses of 100–200 kg, though the fireball still appeared as a single object. At heights of 37–29 km, all primary fragments broke-up again under dynamic pressures up to 5 MPa. The cascade fragmentation then continued, even though smaller pieces breaking off from the larger masses were increasingly decelerated and the dynamic pressure acting upon them decreased. At each fragmentation, a significant part of the mass was lost in the form of dust or tiny particles. This was the dominant process of mass loss. The continuous ablation due to melting and evaporation of the meteoroid surface was less efficient with a corresponding ablation coefficient of only 0.003 $s^2\,km^{-2}$. During fragmentation, some pieces achieved lateral velocities up to 300 m/s, about an order of magnitude more than can be explained by aerodynamic loading. The fragmentation continued even after ablation ceased, as demonstrated by the incomplete fusion crust covering all recovered fragments. We estimate that several hundreds of meteorites of a total mass of ~100 kg landed, mostly in a mountainous area not suitable for systematic meteorite searches. Six meteorites with a total mass of 1.4 kg were recovered up to the end of May 2003. Their positions are consistent with the calculated strewn field.

INTRODUCTION

The fact that meteoroids do fragment during their flight in Earth's atmosphere is well-known (e.g., Ceplecha et al. 1993; Brown et al. 1994). Video records are preferred for fragmentation studies because fragment trails often overlap in classical long-exposure meteor photographs. The videos of the Peekskill fireball and meteorite fall showed extensive fragmentation (Brown et al. 1994) but the trajectories of individual fragments have not yet been extracted from the records. Docobo and Ceplecha (1999) measured several fragments on another fireball video, but the fireball trajectory was partly based on visual data. Here, we report a detailed analysis of the fragmentation of the Morávka fireball and meteorite fall of May 6, 2000. Three video records of the fireball exist and are described by Borovička et al. (2003a), where the fireball trajectory was also determined. The analysis of the video record is supplemented by the analysis

of seismic waves induced by the fireball, which also contain signatures of the fragmentation events. The seismic records were described and interpreted by Brown et al. (2003).

Fragmentation can be studied not only geometrically but also dynamically by using an observed sudden change of deceleration caused by a sudden mass loss. We will apply both the dynamic and geometric methods to the Morávka video data. The results will be compared with other fireballs and with the fragmentation theory. We will also compute the dark flights of the fragments after ceasing ablation, predict the meteorite impact area, and compare it with the positions of the 6 recovered meteorites. The properties of the meteorites, H5–6 ordinary chondrites, were described in Borovička et al. (2003b). Finally, we will compare the global characteristics of the Morávka meteorite fall with other well-documented meteorite falls. However, before analyzing the actual data, we will briefly describe the method used to treat the movement of meteoroid fragments.

DYNAMICS OF ABLATING METEOROIDS

We assumed that the movement of the meteoroid on a segment of the trajectory where no fragmentation occurs is governed by the classical equations for a single body meteoroid. These are the drag equation, the mass-loss equation, and the height equation, which describe the linear trajectory above the spherical Earth's surface. The equations and their solution are given in Ceplecha et al. (1998, pages 349–350) and will not be repeated here. The integral solution enables us to compute the movement of a meteoroid on a given trajectory and its mass loss. The initial parameters to be given are: the time, altitude, and velocity at the beginning point, the ablation coefficient (σ), and the parameter $Km^{-1/3}$ at the beginning. The parameters (σ) and (K) are assumed to be constant. Here, m is meteoroid mass and K is the shape density coefficient. The dynamics only depend on the combination $Km^{-1/3}$. Therefore, to know the mass, we have to estimate the value of the shape density coefficient $K = \Gamma A \rho_d^{-2/3}$. Here, ρ_d is the meteoroid density, which can be set equal to the measured density of meteorites in our case ($\rho_d = 3.59$ g cm^{-3}), Γ is the drag coefficient, and A is the shape coefficient. ΓA was reliably determined by Ceplecha (1996) to be 1.10 ± 0.04 in case of the Lost City fireball. However, the meteoroid was rather flat in that case, and its rotation produced measurable changes in deceleration. For a spherical body, $A = 1.21$. The most probable value of Γ is about 0.7. We will assume an adopted value of $\Gamma A = 1.00$ in all computations. Of course, shapes of different fragments can differ, so the given masses are only approximate.

The trajectory of the fireball is known. Although individual fragments deviate from the trajectory, we will ignore these small deviations in the dynamical calculations and will project all fragments on the mean trajectory. The observations give the position on the trajectory as a function of time. The approach is used to fit the observed data by adjusting the free parameters. Although numerical procedures are available to find the parameters by the least squares method (Ceplecha et al. 1998), this could rarely be applied to the Morávka data. The procedures used are described below.

HIGH ALTITUDE FRAGMENTATION

First, we will study the dynamics of the fireball on the Janov video. This video covers the altitudes 45.7–40.0 km (see Borovička et al. 2003a). The line-of-sight was nearly perpendicular to the trajectory, which is convenient for velocity measurements. The fireball resembles a single object with a nearly circular head and a long tail. The apparent diameter of the head is 0.2°, which corresponds to 300 m. This size can, however, be overestimated due to image saturation. The length of the tail increases from 3.0 km on the first image to 6.3 km on the last image.

The measured positions of the fireball head were fitted to obtain meteoroid dynamic mass. The results of several attempts are given in Fig. 1. The larger mass, the lower initial velocity, and larger ablation coefficient must be assumed to account for the observed velocity decrease. The ablation coefficient, however, cannot be too large, since some substantial mass must still be present at the height of 40 km. One can see that the observations can be explained if the mass at the altitude of 45.7 km was in the range of 100–200 kg. Choosing a mass of 500 kg already gives a strong systematic trend of residuals. The deceleration of the fireball was simply too large to accommodate such a mass.

The conclusion that the initial meteoroid mass was smaller than 200 kg would be in strong contradiction with the initial mass of 1500 ± 500 kg determined from fireball luminosity and infrasound. The discrepancy could be removed by the assumption that $\Gamma A \approx 2$, but that would imply an extremely flat meteoroid (about 5:1). More likely, the meteoroid was already fragmented into 5–10 pieces of similar mass between 100 and 200 kg at the altitude of 46 km. The dynamics were then governed by the mass of single fragments, while the total luminosity and other effects were
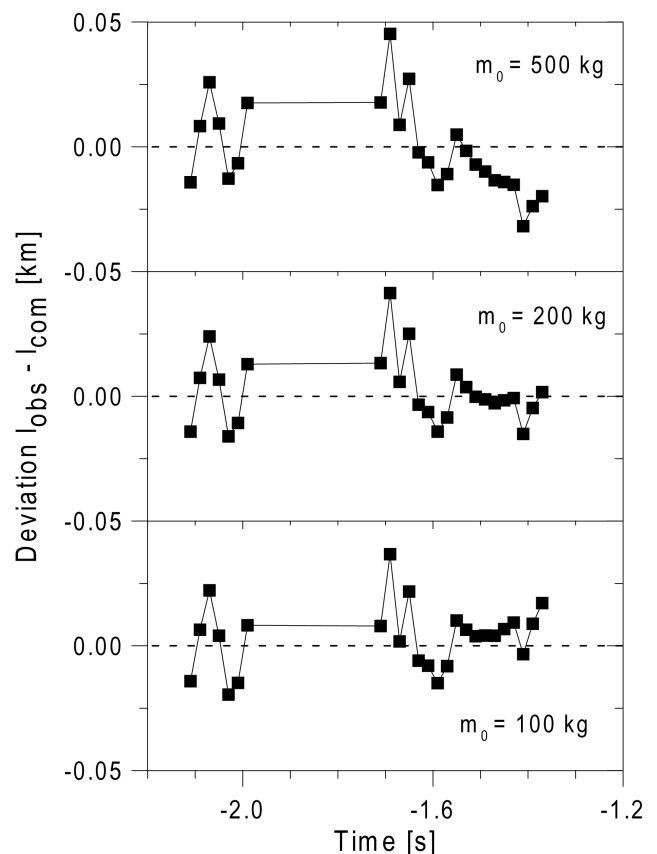

Fig. 1. The differences between observed and computed length along the trajectory as a function of time on the Janov video. The computation was done for 3 sets of parameters, i.e., beginning mass, velocity, and ablation coefficient: 100 kg, 21.92 km/s, 0.002 s^2/km^2 (bottom panel); 200 kg, 21.87 km/s, 0.020 s^2/km^2 (middle panel); 500 kg, 21.82 km/s, 0.040 s^2/km^2 (upper panel). The time is counted from the beginning of the Kunovice video ($\approx$11:51:53 UT).

determined by the summary mass of all fragments. This is the same situation encountered in the case of the Benešov fireball (Borovička et al. 1998). Unfortunately, we are not able to restrict the altitude where this high-altitude fragmentation occurred. It must have been at ~50 km or higher.

This conclusion relating to high-altitude fragmentation is not in contradiction with the appearance of the fireball on the Janov video. The mutual separation of fragments of the masses 100 and 200 kg due to different deceleration will only be a few tens of meters at the altitude of 40 km and, thus, not resolvable on the images. On the other hand, smaller fragments can be hidden in the tail. The breakup of an initial continuous tail into a number of fragments was seen on the Peekskill video and may have occurred here after the end of the Janov video.

LOCATION OF FRAGMENTATION EVENTS FROM SEISMIC DATA

Apart from aerodynamical effects due to the supersonic flight of meteoroids, individual fragmentation events represent sources of sound. The fragmentations are small point-like explosions forming spherical sonic waves. The waves propagate through air to the seismic stations and form a maxima of energy in the part of the seismic record following the first arrival of direct airwaves (see Brown et al. 2003). The identification of an event in the records of several stations enables us to locate the event in the atmosphere from the timing alone. Of course, one must account for variations in the speed of sound as a function of altitude and the wind.

To better compare the strengths of individual events on different stations, the complex amplitude of the signal was recomputed to the standard 10 km range to the source. The correction to the density of energy was also made. The density of energy is proportional to the derivation of the function expressing the length of the trajectory that contributes to the signal during a given time interval. The density of energy is largest at the moment that direct airwaves (from the closest point of the trajectory) first arrive. These corrections were made based on the knowledge of the preliminary fireball trajectory (computed from the first arrival of the direct airwaves) and the coordinates of the station. An example of the corrected amplitude is given in Fig. 2 for station HAV. The example shows a strong event at the range of 42 km and a number of other events.

To identify the events at different stations, the approximate positions on the fireball trajectory of outstanding events seen in some records was computed. Theoretical arrivals of signal from these events to other stations were computed and event signatures searched. After successful identification, improved preliminary location of the events was computed under the assumption of constant speed of sound and no wind. From these locations, ray tracing to the stations was performed, and the average speed of sound and the wind drift were computed from the known temperature

and wind profiles. The locations were then finalized by using the average sound speed and by moving the stations fictitiously by the amount opposite to the wind drift. The final location, therefore, accounted for both the wind field and the change in sound speed with height.

The final location of the events is given in Table 1. The formal errors computed from the residual of timing are on the order of 100 m. The errors could be larger in case of erroneous identification, which cannot be fully excluded for the events early on the trajectory, which were located farther away from the stations. The strength is a relative estimate of the energy of the event. Note that not all fragmentation events are listed in Table 1. A number of smaller events occurred, in particular between the events K and L, that could not be localized because the cross-identification of their signatures in records of different stations was ambiguous.

For example, the identification of seismic events in the records is shown in Fig. 3. Note, however, that only 1 component of the seismic signal is shown in the figure, while the real identification was done from the complex amplitude, i.e., taking into account all 3 components.

The location of seismic events was done completely independently on the video trajectory. The comparison of
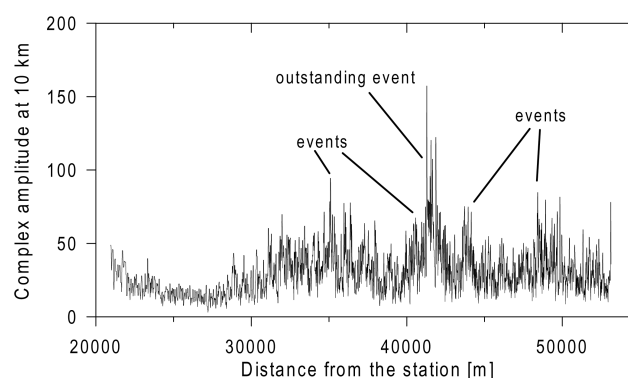

Fig. 2. Deconvoluted seismic signal at station HAV. The complex amplitude corrected to a standard distance of 10 km is given as a function of real distance of the trajectory point from the station.

Table 1. Location of fragmentation events from seismic data.

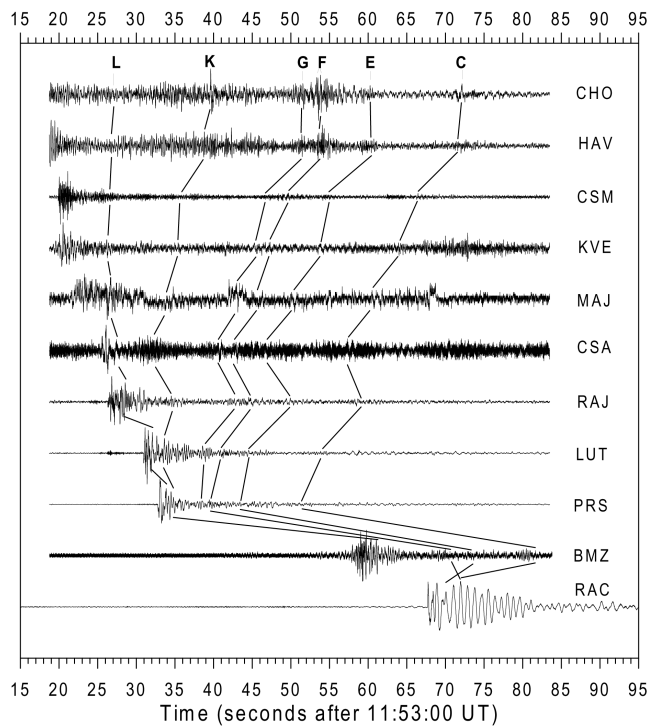| Event	Longitude	Latitude	Altitude	Relative strength (5 = strongest)
A	18.4736	50.0152	36.270	2
B	18.4732	49.9892	35.630	3
C	18.4769	49.9862	35.420	4
D	18.4801	49.9613	34.520	2
E	18.4814	49.9499	33.530	2
F	18.4887	49.9283	32.660	5
G	18.4887	49.9180	32.180	4
H	18.4935	49.8975	31.210	2
K	18.4967	49.8748	30.420	4
L	18.5102	49.8109	28.220	1
M	18.5152	49.7617	26.215	1
N	18.5221	49.7433	25.620	1

Fig. 3. The identifications of some fragmentation events in the seismic records. The vertical component of the seismic signal is shown for each station.

seismically located fragmentation events with the trajectory determined from the video records is, therefore, a useful check of the consistency of both methods. This comparison is done in Fig. 4. The agreement is not bad, although most seismic events lie west of the video trajectory and suggest a different azimuth of the meteor trajectory. The absolute maximum deviation from the video trajectory is 1.3 km for event B. In altitude, the maximum deviation is 0.7 km for events A and H. Most of the events lie below the trajectory. Except for the relatively weak events L, M, and N, the localized fragmentation events occurred on the part of the trajectory not covered by the direct video imaging, above the altitude of 30.4 km.

The scatter in the positions of the seismic events, which is about 1 km, can have 2 causes; either it is a spread caused by location errors, or it is a real scatter caused by secondary fragmentations of different pieces that already followed slightly different trajectories. To check this, we computed the apparent positions (azimuths and elevations) of the located seismic events as they would be seen from Kunovice and compared them with the positions of fragments on the Kunovice video (Fig. 5). We see that the events L, M, and N are well-projected on the swarm of fragments, but the dispersion of the earlier events is too large in comparison with the size of the cloud of fragments. Although these events do not lie in the region covered by the video, we would expect to see some fragmentation products later. Moreover, some
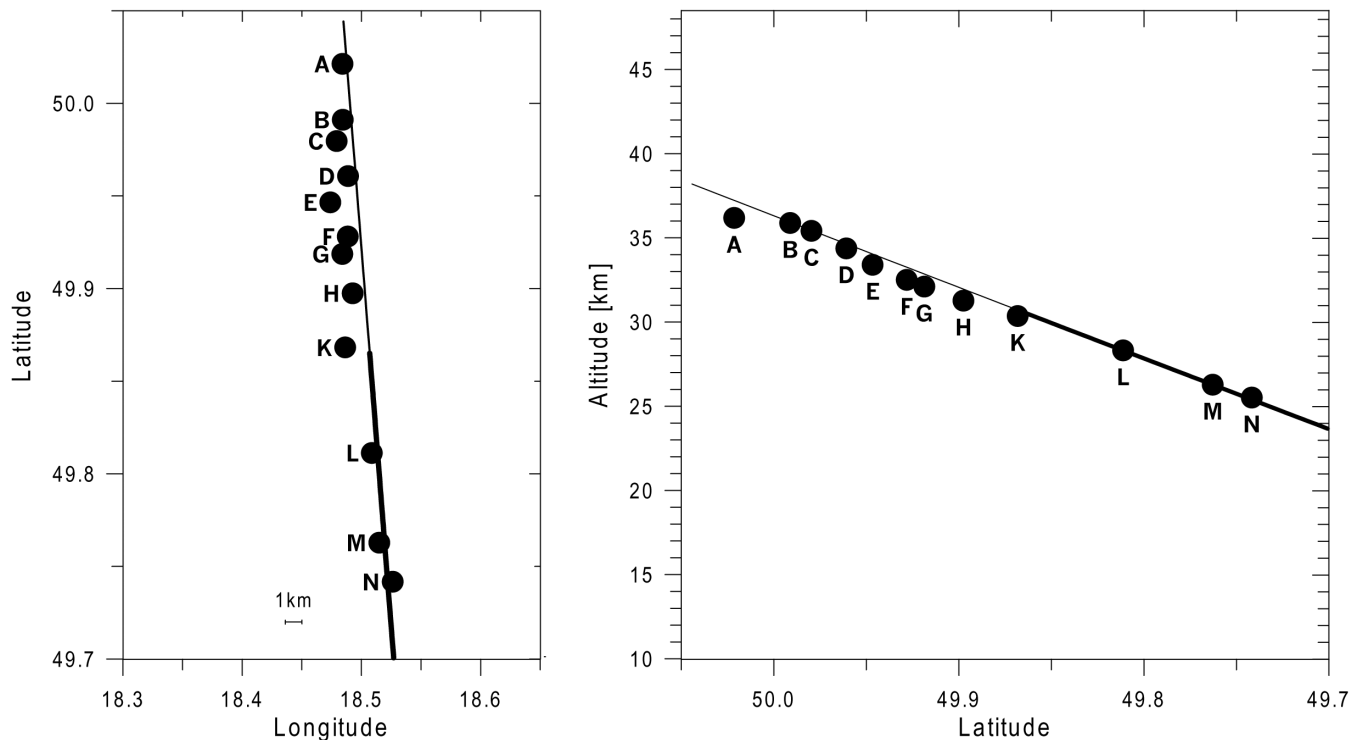

Fig. 4. Location of the seismic events in the longitude-latitude and latitude-altitude plots. The mean trajectory derived from the video records is shown as a thin solid line with a thick segment designating the part of the trajectory seen in the Kunovice video.

fragments, particularly those producing event A, should already be resolved on the Janov video, if the dispersion were so large. Therefore, we conclude that the error of seismic locations of fragmentation events above an altitude of 30 km is at least several hundred meters. Events at lower altitudes seem to be more precisely located, probably due to their occurrances directly above the seismic network.

Although the location of fragmentation events from seismic records proved to be less precise than we had hoped initially, it still provides useful information; it confirms that the most energetic disruptions occurred at altitudes of 37–30 km on the part of the trajectory not covered by video records. No single dominant explosion occurred, but rather a series of events. This is consistent with the concept that the events were caused by disruptions of individual primary fragments that were formed at high altitudes above 50 km. The main series of events (events B–H) occurred between the altitudes of 36–31 km over the trajectory length of 13 km and time interval of ~0.7 sec. This interval probably corresponds to the interval of the clearest signal on the satellite light curve (presented in Borovička et al. [2003a]). The double maximum of the fireball light curve may well correspond to the most energetic event (F), which shows double structure in the seismic data also (Fig. 3).

DYNAMICS OF THE MAIN BODY

The purpose of this section is to describe the dynamics of the main body (i.e., the longest visible fragment) along the trajectory. This means finding the development of its deceleration and mass loss.

We have already solved the dynamics of the fireball on the Janov video. The highly zoomed Kunovice video shows the fireball heavily fragmented and covers the height interval of the main body between 30.6 and 21.2 km (see Borovička et al. 2003a). We will use also the Janov video for the dynamic study. Although individual fragments are not visible on the Janov video, they were so close that the measurements can be used for all of them. However, to use both videos simultaneously, we need to determine the time difference between them. This is not a trivial task. We tried several values until we were able to obtain consistent solutions for all of the studied fragments. We concluded that the Janov video started 2.11 sec before the Kunovice video. The error of this value is 0.005 sec. In the following, we set time zero to the beginning of the Kunovice video.

Only frames with absolute positional calibration are available for dynamic study. On the Kunovice video, these are the frames showing the fireball in the vicinity of clouds. In total, 25 data points from Janov and 41 from Kunovice could be used. To fit the data, we first tried the automatic procedures developed by Ceplecha et. al (1993, 1998). These procedures use the least squares method to adjust the free parameters. The residuals are shown in Fig. 6. The single body non- fragmentation solution (4 free parameters) gave a
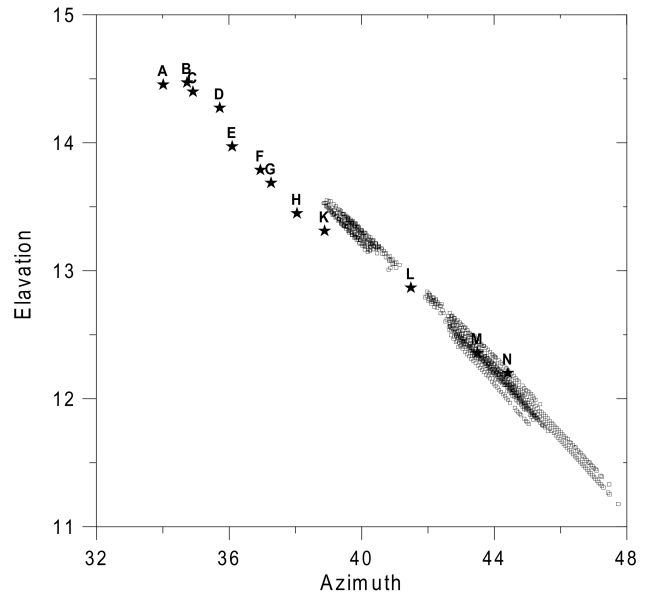

Fig. 5. Celestial coordinates of the located seismic events (asterisks) as seen from Kunovice in comparison with coordinates of individual fragments on the Kunovice video (empty squares). Azimuth is counted from the north here. The scale on the y-axis has been exaggerated.
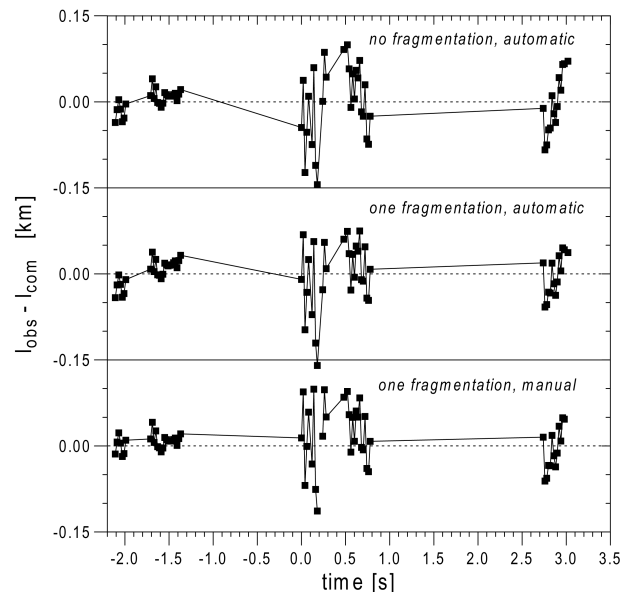

Fig. 6. The differences between the observed and computed length along the trajectory as a function of time for the main body. The residuals are given for 3 solutions: the least squares solution with no fragmentation assumed; the least squares solution with one fragmentation; and the manually adjusted solution with one fragmentation. Numerical values for the last solution are given in Table 2.

systematic trend in the residuals, particularly at the end. The ablation coefficient was 0.011 s^2 km^{-2}, which is close to the typical value of 0.014 s^2 km^{-2} found for type I fireballs corresponding to ordinary chondrites (Ceplecha et al. 1998,

page 422). However, the value of the ablation coefficient is strongly affected by the fragmentation. The one fragmentation solution (5 free parameters) gave better residuals, especially at the end, and the ablation coefficient was only 0.002 s^2 km^{-2}. The residuals at the beginning (on the Janov video), however, still show a systematic trend. Therefore, we manually found (by changing the parameters slightly and looking at the residuals) another solution with a slightly shifted fragmentation point. The manual solution shows the mean residuum around −1.5 sec to be slightly positive (about +10 m). This, however, is quite acceptable because the measurements on the Janov video apply to the center of several fragments. We conclude that the manual solution is best able to explain the observations. The residuals are similar, for both videos, to the residuals of the geometric solution, i.e., in the direction perpendicular to the trajectory (see Borovička et al. 2003a). Therefore, the residuals correspond to the precision of the measurement and calibration.

The parameters of the accepted solution are as follows: the initial mass at the altitude of 45.7 km is 109 kg (for ΓA = 1.0); the initial velocity is 21.90 km/s; and the ablation coefficient is 0.003 s^2 km^{-2} for the whole trajectory. The value of the ablation coefficient (0.003 s^2 km^{-2}) is not very certain; it is near the possible maximum, and the coefficient could be even lower. The model gives meteoroid break-up at 0.23 sec and an altitude of 29.26 km, where the mass decreased from 74.5 to 24.5 kg. In fact, another larger piece was probably formed in this break-up but did not survive long. The 24.5 kg piece continued without significant fragmentation down to an altitude of 21.2 km, where it ceased to be visible on the video. The mass was about 17 kg at that time, and the velocity was 3.8 km/s. Table 2 contains detailed data on the main piece. The observed length is given for all measured points. The computed length, height, velocity, and mass are also given for some intermediate points that are not covered by calibrated observations.

The location of the main body fragmentation at the altitude of 29.3 km places it in the middle between the seismic events K and L. No outstanding seismic event associated with this fragmentation was identified, but seismic records are rich in smaller events in this region. This fragmentation was covered by the video, but no visibly obvious effect is connected with it. However, note that the main body image is overexposed and a moderate change of brightness would be hidden.

LOW ALTITUDE FRAGMENTATION

In this section, we will try to extract as much information on fragmentation as possible from the Kunovice video record. We already showed that the first fragmentation occurred above the altitude of 50 km. From there, an unknown number (probably 5–10) primary fragments in the mass range 100–200 kg flew together. As seismic records show, these fragments started to fragment again at altitudes of ~36 km. The beginning of the Kunovice video shows that the fireball is already heavily fragmented. One primary fragment, however, survived intact down to the altitude of 29.3 km. This fragment was called the main body in the previous section because it finally produced the deepest penetrating body and formed presumably the largest meteorite.

Fragment Numbering and Measurement

The first frames of the Kunovice video are strongly blurred due to camera motion. Fortunately, the sixth half-frame (at 0.10 sec) is reasonably sharp. It is reproduced in Fig. 7. We counted 113 individual fragments on the image. However, this is a very approximate number. Some fragments may not have been resolved. On the other hand, some streaks counted as several fragments may, in fact, just be a wake of larger fragments. The important fact is that the main body (defined above) is not the leading one. The main body is really the brightest one at the time of 0.10 sec, but a number of fragments precede it in the fireball path. In fact, we do not know the exact spatial structure of the fragment cloud because we have an observation from only 1 site. However, that the advance of smaller fragments was just an effect of projection is very improbable. Later, we will show that this advance can be well-explained by the smaller fragments being the fragmentation products of originally larger primary fragments.

Though other frames from the beginning of the video are of a lower quality, we were able to identify a number of fragments (shown in Fig. 7). The positions of the fragments relative to the main body were measured in the x, y system, where x is the coordinate in the direction of flight of the main body (i.e., along the mean video trajectory) and y is perpendicular to the direction of flight. The coordinates, originally measured in pixels, were recomputed to km using the known geometry of the trajectory and the known viewing direction and scale of the video. In this two-dimensional approximation, all fragments were assumed to lie in the vertical plane containing the mean video trajectory. At the time of 0.10 sec shown in Fig. 7, the width of the fragment cloud was about 400 m. The leading fragments were 350 m in front of the main body; fragments 6–8 were 2.9 km behind it. Fainter fragments (not shown in Fig. 7) were up to 4 km behind the main body.

The same measuring procedure was applied to the fireball after its reappearance from behind the cloud. The configuration of the fragments changed significantly in the interim, and each fragment was not immediately distinguishable. An example of a relatively good frame after the cloud is shown in Fig. 8. Fourteen fragments are clearly seen; one more (number 51) is just outside the field-of-view and is visible on the next frame. The fragments were

Table 2. Dynamic data for the main body. For a given time, the following data are given: The observed length along the trajectory, the difference between the observed and computed length, the computed length, altitude, velocity and mass (for ΓA = 1.0).

t (s)	l_obs (km)	o-c (km)	l_com (km)	h_com (km)	v_com (km/s)	m_com (kg)
−2.11	−42.492	−0.014	−42.478	45.700	21.90	109.0
−2.09	−42.033	0.007	−42.040	45.543	21.89	108.9
−2.07	−41.579	0.023	−41.602	45.386	21.87	108.8
−2.05	−41.160	0.005	−41.165	45.229	21.86	108.7
−2.03	−40.746	−0.018	−40.728	45.072	21.84	108.5
−2.01	−40.305	−0.013	−40.291	44.916	21.82	108.4
−1.99	−39.845	0.010	−39.855	44.760	21.80	108.3
−1.71	−33.776	0.012	−33.788	42.588	21.52	106.3
−1.69	−33.317	0.041	−33.358	42.434	21.50	106.1
−1.67	−32.922	0.006	−32.928	42.280	21.47	106.0
−1.65	−32.473	0.026	−32.499	42.127	21.45	105.8
−1.63	−32.072	−0.001	−32.070	41.974	21.42	105.6
−1.61	−31.646	−0.003	−31.642	41.821	21.40	105.5
−1.59	−31.225	−0.010	−31.215	41.668	21.37	105.3
−1.57	−30.791	−0.004	−30.787	41.515	21.35	105.1
−1.55	−30.346	0.015	−30.361	41.363	21.32	104.9
−1.53	−29.924	0.011	−29.935	41.211	21.29	104.8
−1.51	−29.501	0.008	−29.509	41.059	21.26	104.6
−1.49	−29.075	0.009	−29.084	40.907	21.24	104.4
−1.47	−28.651	0.009	−28.660	40.756	21.21	104.2
−1.45	−28.225	0.011	−28.236	40.605	21.18	104.0
−1.43	−27.799	0.014	−27.813	40.454	21.15	103.8
−1.41	−27.389	0.001	−27.390	40.303	21.12	103.6
−1.39	−26.955	0.013	−26.968	40.152	21.09	103.4
−1.37	−26.525	0.021	−26.547	40.002	21.05	103.2
−1.30	–	–	−25.077	39.478	20.94	102.4
−1.20	–	–	−22.992	38.735	20.76	101.3
−1.10	–	–	−20.925	38.000	20.56	100.1
−1.00	–	–	−18.879	37.272	20.35	98.8
−0.90	–	–	−16.856	36.553	20.12	97.4
−0.80	–	–	−14.856	35.843	19.86	95.9
−0.70	–	–	−12.883	35.143	19.59	94.4
−0.60	–	–	−10.939	34.454	19.29	92.7
−0.50	–	–	−9.026	33.776	18.97	91.0
−0.40	–	–	−7.147	33.110	18.62	89.3
−0.30	–	–	−5.303	32.458	18.25	87.4
−0.20	–	–	−3.498	31.820	17.85	85.6
−0.10	–	–	−1.734	31.197	17.43	83.7
0.00	0.000	0.014	−0.014	30.589	16.98	81.8
0.02	0.419	0.094	0.325	30.470	16.89	81.4
0.04	0.593	−0.069	0.662	30.351	16.80	81.0
0.06	0.996	−0.001	0.997	30.233	16.70	80.7
0.08	1.389	0.059	1.330	30.115	16.61	80.3
0.12	1.959	−0.032	1.990	29.882	16.42	79.5
0.14	2.417	0.099	2.318	29.767	16.32	79.1
0.16	2.567	−0.076	2.643	29.652	16.22	78.8
0.18	2.853	−0.113	2.967	29.538	16.13	78.4
0.20	–	–	3.288	29.424	16.03	78.0
0.23	–	–	3.767	29.256	15.88	frgm
0.24	3.942	0.017	3.925	29.200	15.80	24.4
0.26	4.338	0.098	4.240	29.089	15.66	24.2
0.28	4.602	0.051	4.552	28.979	15.51	24.1
0.30	–	–	4.860	28.870	15.36	23.9
0.40	–	–	6.360	28.342	14.63	23.1

Table 2. Dynamic data for the main body. For a given time, the following data are given: The observed length along the trajectory, the difference between the observed and computed length, the computed length, altitude, velocity and mass (for $\Gamma A = 1.0$). *Continued.*

| t (s)	l_obs (km)	o-c (km)	l_com (km)	h_com (km)	v_com (km/s)	m_com (kg)
0.48	7.592	0.085	7.507	27.938	14.05	22.6
0.52	8.158	0.095	8.063	27.743	13.76	22.3
0.54	8.392	0.054	8.337	27.646	13.62	22.2
0.56	8.597	−0.011	8.608	27.551	13.47	22.0
0.58	8.926	0.050	8.876	27.457	13.33	21.9
0.60	9.149	0.008	9.141	27.364	13.19	21.8
0.62	9.464	0.061	9.403	27.271	13.05	21.7
0.64	9.713	0.050	9.663	27.180	12.91	21.6
0.66	10.003	0.084	9.920	27.090	12.77	21.4
0.68	10.171	−0.002	10.174	27.000	12.63	21.3
0.70	10.418	−0.007	10.425	26.912	12.49	21.2
0.72	10.725	0.051	10.673	26.825	12.36	21.1
0.74	10.880	−0.039	10.919	26.739	12.22	21.0
0.76	11.117	−0.045	11.162	26.653	12.09	20.9
0.78	11.411	0.008	11.403	26.569	11.95	20.8
0.80	–	–	11.640	26.485	11.82	20.7
1.00	–	–	13.876	25.700	10.56	19.8
1.20	–	–	15.870	25.000	9.41	19.2
1.40	–	–	17.648	24.377	8.39	18.7
1.60	–	–	19.234	23.821	7.49	18.3
1.80	–	–	20.651	23.325	6.70	18.0
2.00	–	–	21.922	22.880	6.02	17.7
2.20	–	–	23.065	22.480	5.43	17.5
2.40	–	–	24.097	22.119	4.91	17.4
2.60	–	–	25.033	21.792	4.46	17.3
2.74	25.652	0.015	25.637	21.581	4.18	17.2
2.76	25.659	−0.061	25.720	21.552	4.14	17.2
2.78	25.746	−0.056	25.803	21.523	4.10	17.2
2.80	25.851	−0.034	25.885	21.494	4.07	17.2
2.82	25.931	−0.034	25.965	21.466	4.03	17.2
2.84	26.064	0.018	26.046	21.438	4.00	17.2
2.86	26.108	−0.017	26.125	21.410	3.96	17.2
2.88	26.168	−0.036	26.204	21.382	3.93	17.2
2.90	26.270	−0.013	26.282	21.355	3.89	17.2
2.92	26.394	0.034	26.360	21.328	3.86	17.2
2.94	26.445	0.009	26.437	21.301	3.82	17.2
2.96	26.562	0.049	26.513	21.275	3.79	17.2
2.98	26.635	0.047	26.588	21.248	3.76	17.1
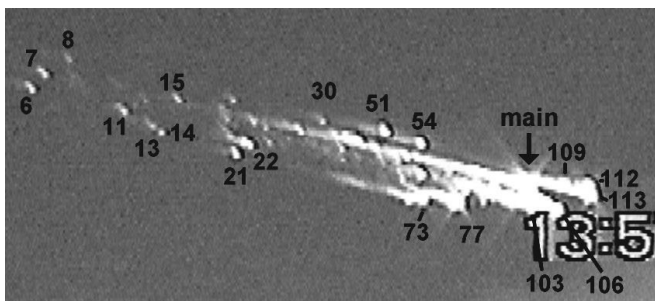
Fig. 7. The image of the fireball at the time of 0.10 sec from the Kunovice video. Some fragments are numbered.
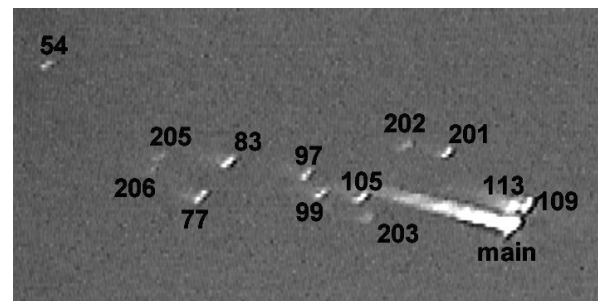

Fig. 8. The image of the fireball at the time of 0.86 sec from the Kunovice video. The fragments are numbered.

numbered after their motion was correlated with the fragments measured before the cloud passage. New fragments (i.e., these formed by break-ups of earlier fragments) were designated by numbers greater than 200.

Fragmentation Sequence

In this section, we will find the genetic relationships of the measured fragments. The determination of the whole fragmentation sequence was done in 2 ways. First, the x, y plot was constructed. The positions of fragments at different times were plotted and fitted with straight lines (Fig. 9). That the fragments do not originate in a single point can be seen easily. The fragmentation procedure was quite complex with many subsequent disruptions. For example, the 2 leading fragments (112 and 113) are products of 1 primary fragment (which we designate as P1), while fragments 106 and 103 are products of another primary fragment (P2).

The second method, by which all potential fragmentations are confirmed and others are found, is the study of the dynamics. For this purpose, the absolute length along the trajectory must be determined for each fragment at each time. We simply subtracted the x-coordinate from the value for the main body from Table 2. In this way, the frames that were not calibrated directly could also be used. The y-coordinate was ignored because the deviation in the y-direction is small in comparison to the forward motion.

The dynamics were studied for all fragments with at least 7 measurements. We tried to use the automatic procedure for single body solution, but it failed in most cases because observations only covered a small part of the trajectory. In cases where the solution was obtained, the ablation coefficient ranged from 0.003 to 0.04 s^2 km^{-2}. Finally, however, the parameters of the fragments and the genetic relationships among them were determined by a trial-and-error method. We adjusted the beginning time, height, velocity, mass, and ablation coefficient of a fragment. Then, the time of the next break-up of the fragment was adjusted. The height, velocity, and mass at that moment were unambiguously defined by the previous parameters. Only the masses and ablation coefficients of the daughter fragments were found. No velocity change at the fragmentation point was assumed. All parameters were adjusted to get the observed minus computed residua of the length with no systematic trends. The fragments with genetic relationships also had to converge in the x, y plot. The ablation coefficient was set to the standard value of 0.003 s^2 km^{-2} unless the observations forced another value. The density of all fragments was set to 3.59 g cm^{-3}, and ΓA was set to 1.0. Note that deviations from the main trajectory were ignored in the dynamic study.
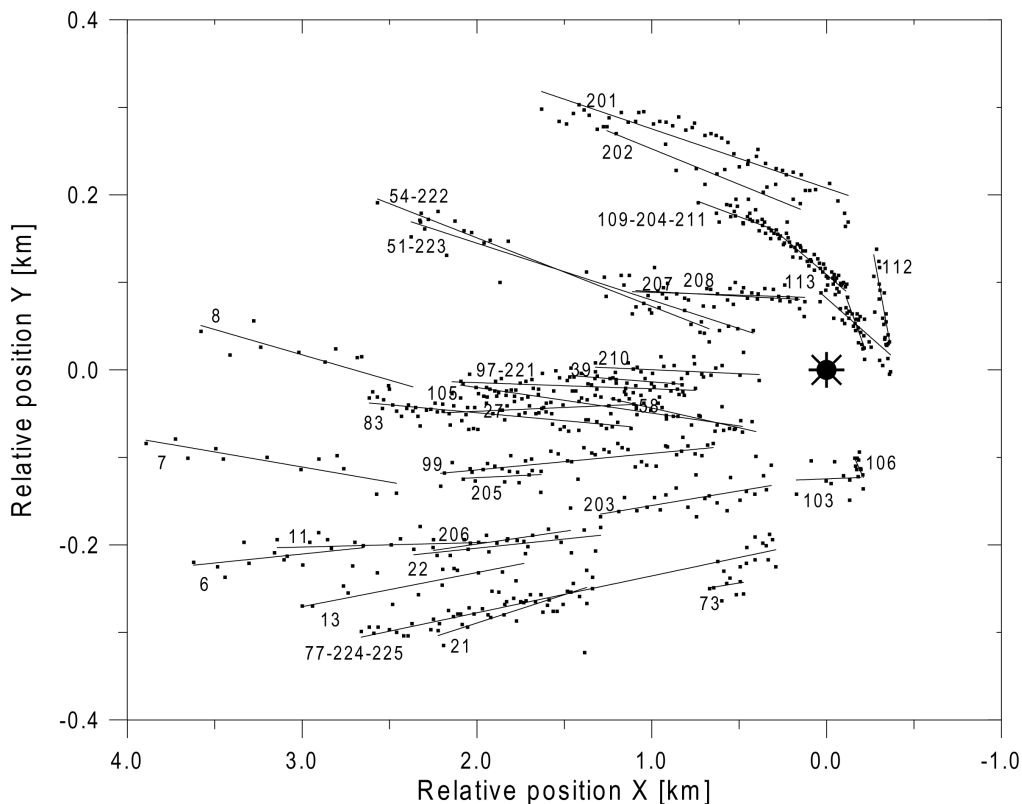

Fig. 9. The positions of the fragments measured relative to the main body (at position 0.0,0.0) in the direction of the flight (x-axis, positive behind the body) and in the perpendicular direction (y-axis). The coordinates are projections onto the vertical plane and are based on the whole Kunovice video. Straight lines are drawn through the positions of individual fragments. The scale on the y-axis has been exaggerated.

The scheme of the fragmentation is shown in Fig. 10. We were able to reconstruct the history of 4 primary fragments. Three of them disrupted shortly before the start of the Kunovice video and formed the fragments that move in front of the main body at the beginning of the video (see Fig. 7). The fourth primary fragment is the main body itself. It is the only primary fragment not yet disrupted at the beginning of the video. All other fragments, which move behind the main body, must be products of other primary fragments that disrupted earlier at heights above 32.5 km. We were not able to reconstruct their history from the video records. Some of these fragments could be measured on sufficient numbers of frames before the cloud passage to estimate their masses. Some others (namely 105, 99, 97, 83) could be measured only after the cloud passage because they were not separated enough from other fragments before the cloud. A few well-separated fragments (77, 54, 51) could be measured both before and after the cloud but the dynamics study showed that they underwent fragmentation in-between. The fragments flying behind fragment 51 were not seen after the cloud, but whether they disappeared because they would be outside the field-of-view is not certain.

One consequence of the complex fragmentation procedure is that the most massive fragment was not always the leading one. The main body was shown to be preceded by several less-massive fragments at the beginning of the Kunovice video. Since less-massive bodies were being more decelerated and all of the fragments fragmented further, several different bodies interchanged in the leading position. The P1 and its product 113 were later interchanged by 204 (of the P3–109–204 sequence) before 200 (of the P4–200 sequence) finally took the leading position. This reconciling was possible only because of the existence of video records. Classical meteor photographs with long exposures and rotating shutters would produce measurements of the positions of the foremost light source without revealing that they are produced by physically different objects. We tried to apply the dynamics analysis of Ceplecha et al. (1993) to the simulated photographic measurement of Morávka. The result was an unrealistic solution, i.e., an "inverse fragmentation" where the mass of the body suddenly increases at one point. This kind of behavior was observed in a number of real photographic fireballs. We suggest that the physical interchange of fragments is an explanation of some, though certainly not all, of these cases. Presumably, this effect can be important in big fireballs with extensive fragmentation and rather shallow trajectories. However, note that a similar effect, when the leading and the brightest fragment A terminated higher than the fainter fragment B, was observed in the Innisfree meteorite fall (Halliday et al. 1981).

Properties of the Fragments

In this section, we discuss the masses and ablation coefficients of individual fragments. The resulting parameters of all dynamically studied fragments are given in Table 3. The
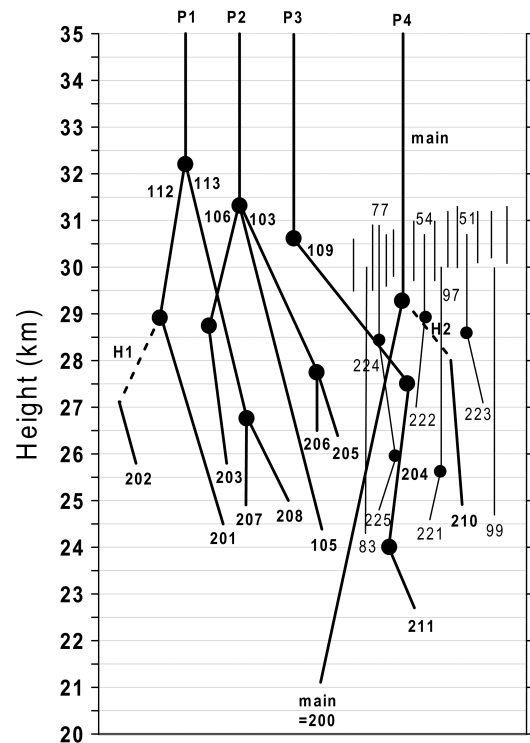

Fig. 10. Scheme of the low altitude fragmentation. The fragmentation history of 4 primary fragments, P1 to P4, is shown. P4 is identical to the main body. The height in km is given on the vertical axis. The position on the horizontal axis is arbitrary. Fragmentation points are marked by full circles and fragment numbers are given. Dashed lines represent hypothetical fragments that were not observed directly. Other dynamically studied fragments, not originating from P1–P4, are shown by thin lines, and their fragmentation points are shown as smaller circles.

height, velocity, and mass at the beginning and the end point of the fragment trajectory and the corresponding times (counted from the start of Kunovice video) are given. The beginning point is either the point where the fragment was first observed or where it was born in a break-up of its parent fragment. The end point is either the point of fragment break-up or the point where the velocity decreased to 4 km/s. We assumed that the ablation stops at this velocity and the fragment continues dark flight and impact. The observation does not usually cover the whole trajectory from break-up to break-up or from break-up to the ceasing of ablation, so the beginning and end values are extrapolated from the middle of the trajectory. The extrapolation was not done for the fragments observed before the cloud passage only because the velocity was still quite high, and we do not know what happened afterward. So, in these cases, the given values are for the actual observed intervals. The ablation coefficient and the number of measurements are given in the last 2 columns. The identification of the parent and daughter fragments (if any) is given in the second column.

In 2 cases, hypothetical fragments not directly observed had to be included into the fragmentation sequences. This was

Table 3. The parameters of the dynamically studied fragments.

No.	Parent / daughters	Time from/to (s)	Height from/to (km)	Velocity beg/end (km s^{-1})	Mass beg/end (kg)	Ablation coefficient (s^2 km^{-2})	N[a]
P1–P4 fragmentation sequence							
P1[b]	–/113,112	–2.11/–0.29	45.7/32.3	21.9/18.6	157/142	0.0015	25[c]
P2[b]	–/106,105,103	–2.11/–0.15	45.7/31.4	21.9/17.9	129/114	0.0015	25[c]
P3[b]	–/109	–2.11/–0.01	45.7/30.6	21.9/17.3	127/106	0.002	25[c]
P4[d]	–/200, H2	–2.11/0.23	45.7/29.3	21.9/15.9	109/77	0.003	34[c]
113	P1/207, 208	–0.29/0.71	32.3/26.8	18.6/11.7	68/8.4	0.020	20
112	P1/201, H1	–0.29/0.25	32.3/29.0	18.6/15.5	43/37	0.003	12
109	P3/204	–0.01/0.57	30.6/27.5	17.3/13.3	29/24	0.003	17
106	P2/203	–0.15/0.33	31.4/28.7	17.9/14.8	33/29	0.003	10
105	P2/impact	–0.15/2.17	31.4/23.6	17.9/4.0	23/3.0	0.0135	47
103	P2/205, 206	–0.15/0.61	31.4/27.7	17.9/10.6	5.7/4.2	0.003	9
H1[b]	112/202	0.25/0.51	29.0/27.8	15.5/12.7	6.1/5.4	0.003	0
H2[b]	P4/210	0.23/0.47	29.3/28.0	15.9/14.4	47/34	0.015	0
200[d]	P4/impact	0.23/3.01	29.3/21.2	15.9/3.7	24.5/17.1	0.003	31
201	112/impact	0.25/2.27	29.0/23.3	15.5/4.0	6.3/4.5	0.003	48
202	H1/impact	0.51/1.85	27.8/24.4	12.7/4.0	1.8/1.4	0.003	16
203	106/impact	0.33/2.03	28.7/24.0	14.8/4.0	3.3/2.4	0.003	22
204	109/211	0.57/1.55	27.5/24.0	13.3/7.2	14.7/12.2	0.003	48
205	103/impact	0.61/1.99	27.7/24.5	10.6/4.0	2.4/2.1	0.003	7
206	103/impact	0.61/1.81	27.7/24.9	10.6/4.0	1.3/1.1	0.003	7
207	113/impact	0.71/1.97	26.8/23.8	11.7/4.0	2.3/1.9	0.003	19
208	113/impact	0.71/1.87	26.8/24.1	11.7/4.0	1.6/1.3	0.003	14
210	H2/impact	0.47/2.05	28.0/23.7	14.4/4.0	3.2/2.4	0.003	18
211	204/impact	1.55/2.51	24.0/22.2	7.2/4.0	7.4/7.0	0.003	28
Other fragment sequences measured on both sides of the cloud							
77	?/224	0.00/0.44	30.7/28.4	16.3/13.0	13.0/11.2	0.003	11
54	?/222	0.00/0.40	30.7/28.8	15.0/12.6	16.5/15.0	0.003	15
51	?/223	0.02/0.46	30.7/28.6	14.5/12.2	20/18.2	0.003	14
222	54/impact	0.40/2.20	28.8/24.2	12.6/4.0	4.0/3.2	0.003	9
223	51/impact	0.46/2.30	28.6/24.0	12.2/4.0	4.7/3.9	0.003	7
224	77/225	0.44/1.12	28.4/25.9	13.0/8.2	6.7/5.8	0.003	19
225	224/impact	1.12/2.28	25.9/23.6	8.2/4.0	4.1/3.8	0.003	20
Fragments measured only after the cloud passage							
99	?/impact	0.70/2.28	27.1/23.4	10.8/4.0	5.4/4.6	0.003	40
97	?/221	0.70/1.14	27.2/25.7	10.9/8.2	8.0/7.4	0.003	22
83	?/impact	0.70/2.58	27.3/22.9	10.6/4.0	9.6/8.9	0.0015	52
221	97/impact	1.14/2.32	25.7/23.3	8.2/4.0	5.1/4.7	0.003	21
Fragments measured only before the cloud passage							
73		0.00/0.18	30.8/29.8	16.5/14.5	4.2/3.8	0.003	10
58		0.02/0.26	30.6/29.5	14.1/11.7	2.0/1.8	0.003	10
39		0.00/0.28	30.9/29.5	15.2/12.7	4.4/4.0	0.003	14
27		0.04/0.30	30.7/29.6	12.9/11.1	3.5/3.3	0.003	10
22		0.00/0.30	31.0/29.7	13.9/11.6	3.3/3.0	0.003	15
21		0.00/0.28	31.1/29.8	14.1/12.2	6.2/5.8	0.003	14
13		0.00/0.28	31.2/30.0	13.0/10.5	1.2/1.1	0.003	13
11		0.00/0.28	31.3/30.1	13.2/10.5	0.95/0.86	0.003	13
8		0.06/0.30	31.1/30.1	12.6/11.0	3.0/2.8	0.003	10
7		0.06/0.30	31.1/30.2	12.0/9.9	0.80/0.75	0.003	11
6		0.06/0.30	31.2/30.1	13.4/11.7	4.0/3.8	0.003	12

[a]Number of measurements.
[b]A hypothetical fragment, not directly observed.
[c]25 measurements were taken from the Janov video (the same data for all P fragments).
[d]This fragment is called the main body.

the case for the situation where newly born fragments could not be linked dynamically to previously observed fragments but could be linked geometrically (in the x, y plot). The hypothetical fragments were designated H1 and H2. The reason that they were not seen is that they existed only briefly during the period when the fireball was hidden behind the cloud.

The standard value of the ablation coefficient of $0.003 \ s^2 \ km^{-2}$ was satisfactory in most cases. Some fragments with longer observation series, however, showed larger ablation coefficients. In some cases, this was determined to be a consequence of their additional break-ups along the way. These break-ups were found only dynamically because no other products of them were seen. They were revealed simply as a sudden decrease of mass. The mass must have been lost in the form of fine dust or fragments much smaller than the continuing piece. However, in the case of fragment 109, the existence of 2 fragmentations could also be confirmed by the change of the direction of the movement in the x, y plot (Fig. 9). The fragmentation sequence was designed as 109–204–211. Another similar sequence is 77–224–225.

For some fragments, namely 105 and 113, the larger ablation coefficient could not be explained by individual fragmentations. Therefore, the dynamics was described by ablation coefficients of 0.0135 and 0.02 $s^2 \ km^{-2}$, respectively. Nevertheless, we believe that some kind of fragmentation is responsible for this enhancement of ablation—probably a series of smaller losses of mass in the form of tiny pieces and dust. On the other hand, the dynamics of fragment 83 pointed out a very small ablation coefficient of $0.0015 \ s^2 \ km^{-2}$ (or less). Such a small ablation coefficient was also assumed for primary fragments P1 and P2 to achieve their separation from P4. All this analysis suggests that the ablation coefficient on the part of trajectories with no fragmentation or instantaneous mass loss was in the range of only $0.001–0.003 \ s^2 \ km^{-2}$.

The dynamical analysis also provided the estimates of fragment masses. At the time of 0.10 sec (Fig. 7) the mass of the main body was 80 kg. The fragments preceding the main body had mostly 30–40 kg (fragments 106, 109, 112, 113), but fragment 103 was much smaller (5 kg). Other relatively big fragments are 51 (20 kg), 54 (16 kg), and 77 (12.5 kg), while the mass of fragment 73 was only 4 kg. The trailing fragments 6 and 8 were bigger (4 and 3 kg) than nearby fragment 7 (0.8 kg). The summary mass of all measured fragments is 310 kg, so the total mass of all fragments was still several hundred kilograms. At the time of 0.86 sec (Fig. 8), the mass of the main body was 20 kg; fragment 109 (in fact, 204 already) had 14 kg. The other relatively big bodies were 83 (9 kg), 97 (8 kg), and 77–224 (6 kg). Fragment 113 was already fragmented into two pieces (207 and 208) of masses of only 2 and 1.5 kg. The masses of other visible fragments ranged from 1 to 5 kg. The total mass of all visible fragments was almost 100 kg. Note that all masses are computed for $\Gamma A = 1.0$.

The Process of Fragmentation

In this section, we will study the fragmentation events statistically, from the point-of-view of relative masses of daughter fragments, acting dynamic pressures, and acquired side velocities. Table 4 contains the parameters of individual fragmentation events studied dynamically. The height and time of the fragmentation, the mass of the parent fragment, and the number and masses of the daughter fragments are given. Also, the mass of the largest daughter fragment relative to the mass of the parent body and the percentage of the mass lost in the fragmentation (i.e., the mass not continuing in the form of daughter fragments) are given. The lost mass was presumably released in the form of dust or very small fragments (<<1 kg). The percentage values are not given for fragmentations that involve fragments H1 and H2, which were not observed directly. Finally, the dynamic pressure acting on the fragment at the time of fragmentation is given. The pressure was computed simply as $p = \rho v^2$, where ρ is the density of the atmosphere and v is fragment velocity. The actual pressure may be lower by the factor (Γ), but the value of the drag coefficient (Γ) is not known, and we ignored it because it is of the order of unity.

The comparison of the dynamically located fragmentations with the locations of the seismic events yielded no clear correlation. Fragmentation F-P3 may correspond to the seismic event K, and F-P1 and F-P2 possibly to G and H, but the differences exceed 1 km. The closest fragmentations to the events L, M, and N are F-77, F-224, and F-97, respectively. But, their correspondence is not convincing. However, note that the seismic record contains many more fragmentation events than those that could be localized.

In Fig. 11, the distribution of the parameters of the fragmentations is shown. The number of continuing macroscopic fragments was generally low, only 1 or 2 in most cases, but is never 0. We did not observe a complete disintegration of a meteoroid, where all the mass would be pulverized. The masses of the largest continuing piece are in a wide range from 12% to 71% of the original mass. Cases with even larger percentages certainly exist, but they cannot be recognized as fragmentations because the change of mass is too small. The absence of cases with fragments smaller than 10% of the original mass is more significant. This shows that neither complete pulverization nor a disintegration into fragments at an order of magnitude smaller than the original piece ever occurred. Also, the percentage of disappearing mass shows a wide distribution, but the extremes near 100% and 0% are absent. The former absence corresponds with the lack of pulverization. The latter shows that splitting into 2 or more pieces along a crack with no release of dust was not typical. We note that the F-P4 fragmentation, which was not well-documented, suggests only 7% of the disappeared mass. Nevertheless, some dust (or tiny fragments) seems always to have been released. Often, the dust comprised more than 50% of the original mass.

Table 4. The parameters of individual fragmentation events.

Event	Height (km)	Time (s)	Parent mass (kg)	nf	Daughter masses (kg)	Largest daughter's mass	Disappeared mass	Dynamic pressure (MPa)
F-P1	32.3	−0.29	142	2	68 + 43	48%	22%	4.3 ↑
F-P2	31.4	−0.15	114	3	33 + 23 + 5.7	29%	46%	4.5 ↑
F-P3	30.6	−0.01	106	1	29	27%	73%	4.8 ↑
F-P4	29.3	0.23	77	2	47? + 24.5	–	–	5.0 ↑
F-112	29.0	0.25	37	2	6.3 + 6.1?	–	–	4.9 ↑
F-54	28.8	0.40	15	1	4.0	27%	73%	3.4 ↓
F-106	28.7	0.33	29	1	3.3	12%	88%	4.8 =
F-51	28.6	0.46	18	1	4.7	26%	74%	3.2 =
F-77	28.4	0.44	11.2	1	6.7	60%	40%	3.8 ↓
F-103	27.7	0.61	4.2	2	2.4 + 1.3	57%	12%	2.8 ↓
F-109	27.5	0.57	24	1	14.7	61%	39%	4.6 ↓
F-113	26.8	0.71	8.4	2	2.3 + 1.9	27%	54%	4.0 ↓
F-224	25.9	1.12	5.8	1	4.1	71%	29%	2.2 ↓
F-97	25.7	1.14	7.4	1	5.1	69%	31%	2.3 ↓
F-204	24.0	1.55	12.2	1	7.4	61%	39%	2.3 ↓

The histogram of dynamic pressures shows that a clear limit exists at 5 MPa. No fragment survived higher pressure without further disruption. Five MPa seems to be the limit of meteoroid strength. The typical material strength of stony meteorites is 2–50 MPa (Bronshten 1983). Here, the strength of the primary fragments was at the lower part of this range. The internal cracks, which are also partly visible in the recovered meteorites, likely are responsible for the relatively low strength of the Morávka meteoroid. However, the high altitude fragmentation, which occurred under the pressures of 0.5 MPa or less, requires that the primary fragments were even more loosely bound together.

After the primary fragments disrupted, their products experienced progressively lower dynamic pressures as they were decelerated. Nevertheless, further fragmentations occurred even during this phase. In Table 4, the sign shows whether the fragmentation occurred during the increase (↑), decrease (↓) or constant (=) dynamic pressure. Many subsequent break-ups occurred at lower pressures than the previous fragmentations of the same body (e.g., in the sequence P3–109–204–211). This means that fragments were predisposed to further fragmentation, which occurred only after some time. We can only speculate about detailed physical processes. These may involve rotation of the body, increasing thermal stress, etc.

We have also studied the velocities acquired by fragments in the direction perpendicular to the trajectory. Instead of using the dynamically derived break-ups, we simply evaluated the velocities of all measurable fragments existing at the time of 0.10 sec (see Fig. 7). This provided more data. The side velocity was determined as a linear dependency of the y-coordinate in the x, y plot on time. In fact, the obtained velocities are only lower limits since the component along the line of sight is not included. The resulting histogram for 27 fragments is in Fig. 12. The number of fragments with side velocities near 0 is underestimated because numerous fragments following nearly the same trajectory could not be measured individually. Nevertheless, some fragments exhibited velocities of about 300 m/s. The largest value is 310 ± 30 m/s for fragment 112. Whether or not all velocities were acquired after only 1 fragmentation event is unclear. However, for fragment 112, the precursor seems to break-up near the main trajectory (see Fig. 9). Therefore, we conclude that side velocities up to 300 m/s were acquired during fragmentation.

COMPARISON WITH OTHER FIREBALLS AND THE THEORY

Morávka is not exceptional by its extensive fragmentation in the atmosphere. The falls of ordinary chondrites often occur in large numbers, sometimes approaching 1000 as in the case of Mbale (Jenniskens et al. 1994). The previous 4 ordinary chondrite falls that were instrumentally recorded all showed some degree of fragmentation. In particular, several stages of fragmentation into dozens of fragments was seen in the video record of the Peekskill fireball. Details were not studied, but the lateral displacement reached ~1 km for some small fragments (Beech et al. 1995). The fragmentation occurred under dynamic pressures of 0.7–1 MPa (Ceplecha et al. 1996).

Another video-observed fireball was described by Docobo and Ceplecha (1999). Only 1 video record exists and the geometry was determined by combination with visual data. The trajectory was similarly shallow as in the case of Peekskill. Thirteen fragments were seen to separate from the main body. Although measurements were difficult, lateral velocities of some fragments of ~200 m/s (comparable to those observed in Morávka) are likely. The dynamic pressure at fragmentation was about 1 MPa.

The range of dynamic pressures under which photographically observed fireballs were found to break up
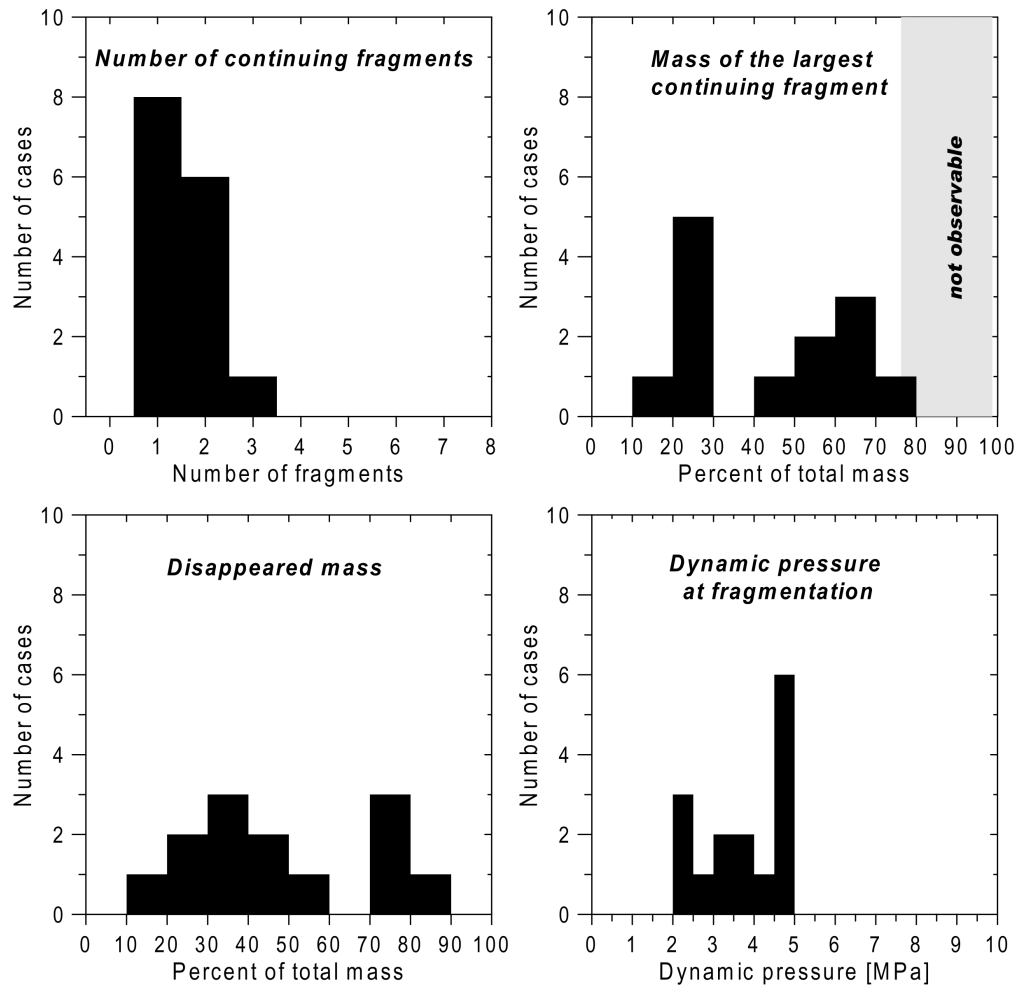
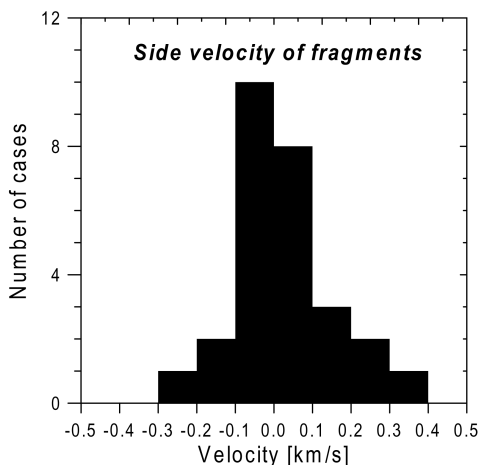Fig. 11. Four histograms showing the distribution of fragmentation parameters.

Fig. 12. Distribution of velocities perpendicular to the trajectory of the measured fragments at 0.10 sec with standard error of 0.04 km/s.

are 0.05–1.2 MPa (Ceplecha et al. 1993, 1998 page 424). So, the "hidden" high altitude fragmentations revealed in Morávka and also in Benešov (Borovička et al. 1998), which

needed about 0.5 MPa, are not exotic. All observations suggest that typical meteoroids are highly fractured when they enter the atmosphere and are ready to break-up under low pressures (although a possible role of turbulence in enhancing the dynamic pressure was noted as an alternative explanation by Foschini [2001]). Models that ignore this fact and apply the strength of meteorites to incoming meteoroids fail to correctly predict the behavior of meteoroids in the atmosphere. For example, the model of Hills and Goda (1993) predicts no fragmentation for a body with Morávka parameters (hard stone, an initial velocity of 22 km/s, and a radius of 0.5 m). Maximal magnitude is predicted to be about −16 and the height at which half of the energy has been deposited is computed to be 26 km. In reality, the ablation was almost completed and the velocity already decreased to 50% of its initial value at this height.

We were able to study the details of the low altitude fragmentation of Morávka, and the data can be compared to existing theories. The most elaborated model of meteoroid fragmentation applicable to Morávka was published by Artemieva and Shuvalov (2001). They computed

hydrodynamic and radiative forces acting on separating fragments, taking into account ablation and radiation. The repulsion velocity of the fragments were expressed in the form:

$$U = V\sqrt{C\frac{\rho_a}{\rho_m}} \qquad (1)$$

where V is the fireball velocity, and ρ_a and ρ_m are the densities of the atmosphere and the meteoroid, respectively. The constant (C) was found to be ~0.2 in the case of fragmentation into 2 pieces and ~1 in the case of fragmentation into a large number of pieces (>10). A model of successive meteoroid fragmentation was created. In this model, fragmentation into 2 non-equal pieces (with random size ratios) occurs when the dynamic pressure exceeds the strength of the i-th generation fragment computed as:

$$\sigma_i = \sigma_0(m_0/m_i)^{1/4} \qquad (2)$$

where σ_0 and m_0 are the meteoroid pre-entry strength and mass, and m_i is the fragment mass. In fact, not only was this nominal strength selected, but also a random value inside a normal distribution factor of 2 around the nominal strength. The model was applied to the observational data of the Benešov fireball taken from Borovička et al. (1998). Reproducing the observed deviations of some fragments from the main trajectory was difficult with this model. In only 1 of ~100 runs was a picture found that was similar to the observations.

In view of the Morávka observations, we see that the model has serious shortcomings. The side velocity computed from Equation 1 for a fragmentation at the height of 32 km is only 15 m/s. Even if we take C = 1 (and we have no reason to do so given that we do not observe disruptions into a large number of pieces), the predicted velocity is still only 35 m/s. The observed values go up to 300 m/s, and although this is an extreme, velocities of 50 m/s are quite normal.

The second problem is that Equation 2 assumes that the strength of the daughter fragments is always larger than the strength of the parent. This is a common assumption used in meteoroid fragmentation theories (e.g., Baldwin and Sheaffer 1971; Stulov and Titova 2001). However, we have shown that the real behavior was different in the case of Morávka. Fragments did break-up under lower pressures than were present when they were formed. The fact that all recovered meteorites have significant parts of their surfaces without fusion crust shows that the fragmentation continued even after the bodies were decelerated under the velocity at which ablation ceases (i.e., 2–3 km/s). Therefore, the use of Equation 2 must lead to an incorrect prediction of the mass distribution of fallen meteorites. The model also oversimplifies by assuming that the sum of the masses of the daughter fragments is equal to the mass of the parent. We have shown that part of the mass (often more than 50%) is always lost. We believe that the model correctly describes the hydrodynamic interaction of fragments. The observed discrepancies are probably due to the poorly understood properties of meteoroids themselves. The fragmentation process seems to be quite energetic and seems to provide significant impulse to the fragments. The detection of fragmentation events in seismic data also suggests that these processes are similar to small explosions. The process also seems to affect the internal structure of the surviving bodies, making them prone to further fragmentation under lower pressures.

THE SPARKS

Looking at the details of the Kunovice video, we see another phenomenon besides normal fragmentation. This is shown in Fig. 13. Because of the combination of camera movement (shaking) and the motion of the fragments, the fragments are imaged as bars. The orientation (slope) of the bars is slightly different for fragments of different velocities. However, in addition to the fragments, bars with quite different orientations are visible on many frames (other examples can be seen in Fig. 8). These are different kinds of luminous objects that move rapidly backward from the fragments. Their existence is confirmed by the view of some of them on 2 consecutive frames. We tentatively call these objects "sparks" since many visual descriptions of bright fireballs include sparks.

Sparks occur exclusively behind (i.e., in the wake of) macroscopic fragments. The measurement of the sparks seen in Fig. 13 yielded a typical velocity relative to the main body of about −8 km/s. Since the velocity of the main body was 10 km/s, the sparks moved with the velocity of ~2 km/s relative
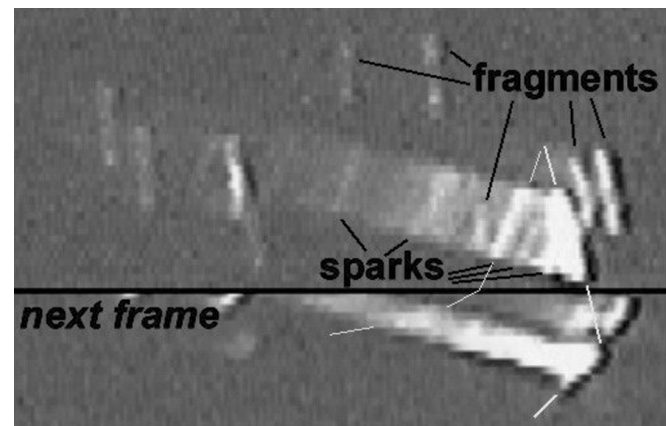

Fig. 13. Fragments and sparks on the Kunovice video. Parts of 2 consecutive blurred half-frames are shown. The main fragment and the brightest spark are identified on both frames by white lines.

to the ambient atmosphere. No significant spark deceleration was observed. The sparks disappeared within 500 m behind the body; therefore, their duration was relatively short (≤0.06 sec).

We interpret the sparks as tiny fragments or liquid droplets that were decelerated quickly after the ablation from the parent body but then managed to escape into the wake. Since they are protected from the incoming atmosphere in the wake, deceleration does not continue and slow evaporation enables them to survive for some period of time, until they reach too large a distance from the protecting fragment.

DARK FLIGHT AND IMPACT

After individual pieces of the fragmented meteoroid were decelerated significantly, ablation stopped, and the fragments continued their so-called dark flight on ballistic trajectories until they impacted the ground. Knowing the position, velocity, and deceleration at the end of the luminous trajectory, the dark flight can be modeled by the procedure described in Ceplecha et al. (1998, page 390). The procedure takes into account atmospheric drag, horizontal winds, and Earth's gravity and rotation. Since the actual shape of the meteoroid is not known, a spherical body is assumed.

The Main Body

The main fragment ceased to be visible on the video at a height of 21.2 km when the velocity was 3.8 km/s and deceleration was −1.6 km/s^2 (according to the solution in Table 2). We started the dark flight calculation from this point. The resulting impact point lies 17.8 km farther in the direction of the flight and 0.18 km west off the trajectory prolongation (due to the prevailing easterly winds; see Brown et al. 2003). The geographical coordinates of the point are 18°33′02″ E and 49°28′57″ N. The calculated impact occurred 130 sec after the fireball ended with an impact velocity of 100 m/s. The calculated height, velocity, and elapsed time during the dark flight are shown in Fig. 14.

To learn more about the fireball near the endpoint, a large number of interviews were performed in the area. The witness reports agree that the main fragment was visible from close sites about 4–5 km further south of the video terminal point. Here, the calculated velocity was 2.0 km/s and the height was 19.5 km. The reports of sonic booms point to the arrival from overhead up to ~8 km south of the video terminal point. Further south, the sounds were reported to have come from a northern direction. This suggests that the meteoroid velocity decreased below the speed of sound at the distance of ~8 km from the terminal point observed on the video. The dark flight calculation yielded a distance of 13 km and a height of 16 km for deceleration below the speed of sound relative to the video terminal point. Therefore, the main fragment was apparently decelerated more than expected. The reason could be additional fragmentation. None of the recovered meteorites
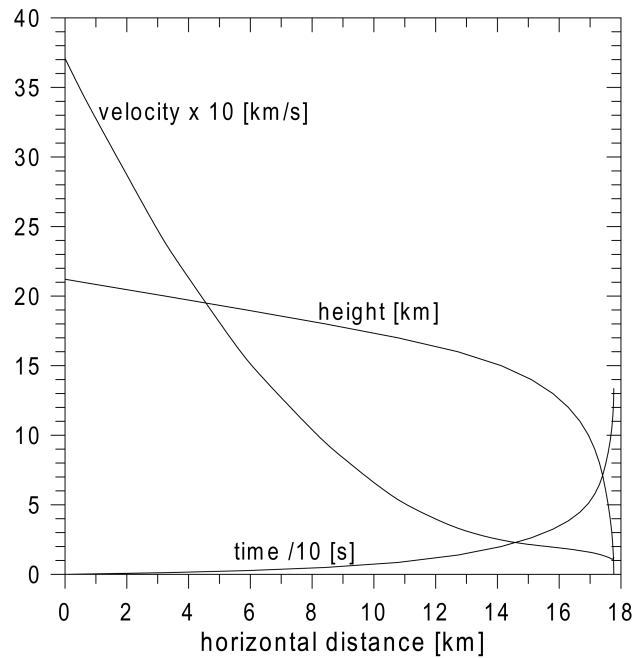

Fig. 14. The calculated velocity, height, and elapsed time as a function of horizontal flight distance during the dark flight of the main fragment. The horizontal distance is counted from the end of the video record.

show complete fusion crust coverage. So, fragmentation after the end of ablation was common. If the main body was fragmented, the fragments landed to the north of the calculated position for the main body.

In principle, the point of the deceleration below the speed of sound could be calculated from the seismic data, namely from the first arrival of the air-coupled P-waves at different stations. However, the P_{term} waves were well detected only on station MORC (see Brown et al. 2003). Station MORC lies in a horizontal distance of 77.5 km from the point where the velocity decreased below the speed of sound according to the dark flight calculation. The P_{term} wave arrived to the station at 11:53:05.3 UT. The speed of sound is 4200 m/s in the upper sedimentary layers or 6200 m/s in the underlying bedrock. Therefore, the first airwaves reached the ground between 11:52:47-53. The meteoroid is modeled as having reached the subsonic point at 11:52:10 (14 sec after the end of the video). So, there are 37–43 sec for the sound to reach the ground. This transforms to the height of the subsonic point being 11–13 km. The dark-flight calculated value is 15.8 km. In fact, the calculated vertical velocity of the meteoroid was lower than the speed of sound starting from the height of 17.4 km at the time 11:52:03. So, the first airwaves to arrive to the ground should be from that point. Nevertheless, a discrepancy of 7 sec or 2 km in height still remains. This discrepancy will not disappear if we assumed that the meteoroid was fragmented and decelerated sooner because this would push the solution higher. Thus, either the meteoroid followed a somewhat lower trajectory than calculated after the end of ablation (e.g.,

because of highly irregular shape) or (more probably) the sound propagation through the air and the rock was slightly different than assumed.

Smaller Fragments and Their Mass Distribution

The dark flight computation was performed for all fragments in Table 3 with predicted impact and also for those observed only before the cloud passage. In total, 28 fragments were evaluated. Of course, in many cases, the extrapolation was large, and further fragmentations may have occurred after the fragment disappeared from the field of view. Moreover, we do not know the complete geometry of the fragments because observations are available from only 1 station. Nevertheless, these computations were not meant to determine the actual impact points of individual fragments but only to map the probable extent of the strewn field. For each fragment (except the main one), 7 geometrical solutions consistent with the observed projection to the vertical plane were constructed and 7 dark flight trajectories were computed. The resulting impact positions are plotted in Fig. 15.

The predicted fall area embraces the recovered meteorites well. Since very small fragments were not seen on the video, no predicted impact points exist in the vicinity of the smallest meteorite #3 (90 g). Nevertheless, this meteorite lies in the northward extrapolation of the fall area despite showing the largest westward displacement from the trajectory. A clear mass sorting of the calculated impact positions exists. However, the recovered meteorites are much smaller than the model masses which correspond to their position. One reason for this discrepancy may be that the calculated dynamic masses of the fragments were done using the assumption of the drag and shape coefficient product $\Gamma A = 1.0$. If $\Gamma A = 0.8$ were used, all masses will drop to 50% without changing the impact positions. This could put the largest meteorite (0.33 kg) nearly into agreement with calculation. However, the other 4 meteorite fall locations will still disagree. The reasons may be additional fragmentation after the cessation of ablation (as demonstrated by the incomplete fusion crust coverage), irregular shapes of the meteorites, and the complexity of the fragmentation process. We cannot study this problem in more detail because only a small minority of all meteorites was recovered.

Estimating the total mass of fallen meteorites is difficult. The sum of the masses of the 29 computed fragments is 106 kg if we assume that $\Gamma A = 1.0$. Since the masses of the recovered meteorites suggest that $\Gamma A = 0.8$ was more appropriate for the terminal parts of the fireball, the sum is reduced to 53 kg. The cumulative mass distribution of the fragments is shown in Fig. 16. The total mass of fragments within a logarithmic interval of 0.25 in mass, as well as all larger fragments, is shown. The distribution is valid for the time at which ablation ended. Additional fragmentation later on could change the meteorite mass distribution on the ground.
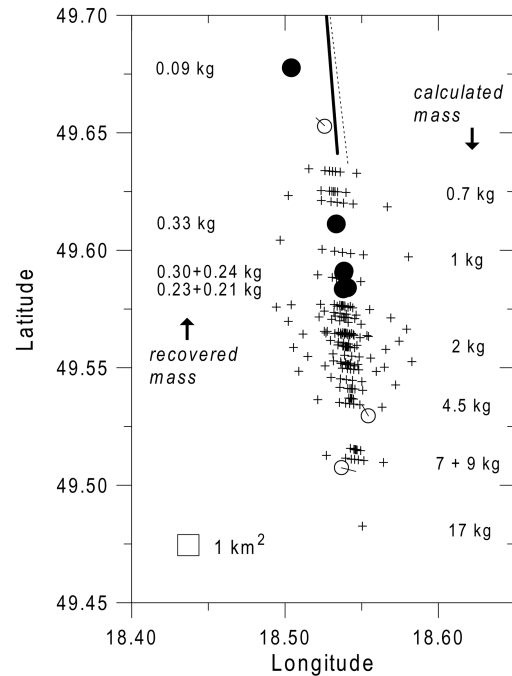

Fig. 15. The possible impact points of individual meteoroid fragments (crosses, 7 solutions per fragment) and the positions of recovered meteorites (full circles, see Borovička et al. [2003a] for coordinates). The masses of the meteorites and the computed masses of the fragments are shown on both sides. The empty circles mark the locations where a meteorite fall was heard but no meteorite was recovered. The short dashes indicate the directions from which the sound of falling meteorite reportedly arrived. The bold line is the ground projection of the fireball video trajectory. For comparison, the trajectory extrapolated from the locations of the seismic events (Fig. 4) is shown as a thin dotted line.
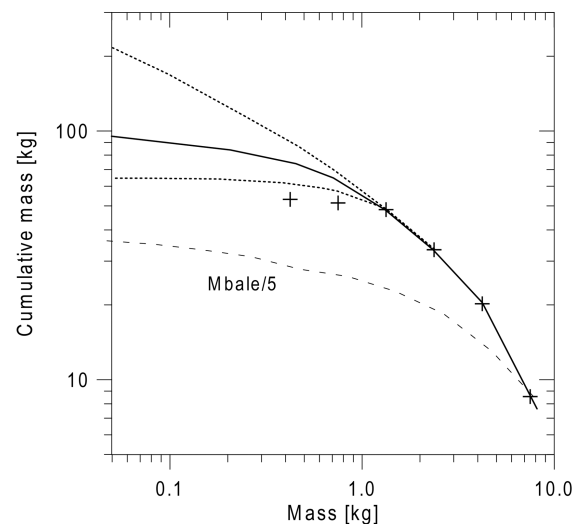

Fig. 16. Cumulative mass distribution at the end of ablation of the dynamically studied fragments (for $\Gamma A = 0.8$, crosses) and the estimated complete distribution (solid line) and its limits (dotted lines). The mass distribution of the Mbale meteorite shower (Jenniskens et al. 1994) is also shown. All Mbale masses were divided by 5 (dashed line) to bring the curve to the same range with Morávka.

Figure 16 shows that the mass distribution does not follow a single power law. Our sample is clearly incomplete for fragments smaller than 1 kg. However, if we extrapolated the distribution in the 1–5 kg range, the total mass would be too large (600 kg for fragments larger than 50 g) in comparison with the meteoroid initial mass (~1500 kg). A better estimate was made using the fact that ≈100 fragments were seen on the video before the cloud passage and assuming that the terminal masses of the fragments that could not be followed after the cloud passage were in the 0.2–1 kg range. This best estimate of the distribution is shown as a solid line in Fig. 16, while the possible limits that we consider to be reasonable are shown as dotted lines. The best estimate of the total fallen mass is 100 kg with possible limits of 60–250 kg. About 50 kg was produced by fragments larger than 1 kg at the end of ablation.

When we compare the Morávka mass distribution to that of the well-studied Mbale meteorite shower (Jenniskens et al. 1994), we see that the Mbale cumulative distribution is flatter at large masses (Fig. 16). The reason is that there were several meteorites of comparable mass to the largest piece (40 kg) in Mbale, while we expect 1 dominant meteorite in Morávka (8 kg).

The total recovered mass is only 1.4 kg. This, however, is quite understandable because most of the strewn field is mountainous and heavily forested (Fig. 17). Five of 6 recovered meteorites were found by chance in the close vicinity of houses and/or on roads. Searches on easily accessible fields, which covered only a tiny fraction of the total area, yielded only 1 meteorite. Other searches were done close to the sites where the characteristic whistling noises that indicate the fall of a meteorite were reported. The locations of the sites are indicated in Fig. 15. The result of this effort was negative. The difficult terrain and uncertain distance between the observer and the impact point are the likely reasons.

GLOBAL CHARACTERISTICS OF THE METEORITE FALL

In this section, we summarize the main data on the Morávka meteorite fall and compare them with the data of 5 other instrumentally imaged falls of chondrites. The comparison is done in Table 5. Data for Pribram, Lost City, Innisfree, Peekskill, and Neuschwanstein were compiled from the literature. However, the meteoroid initial masses were reconsidered because the different methods gave different results in the past. For Pribram, we took the total radiated energy equivalent of 2.3×10^7 zero magnitude stars in 1 sec of Ceplecha (1961), recalculated it to 2.5×10^{10} J, assumed the same 9% luminous efficiency as for Morávka, and arrived at the initial mass of 1300 kg. This is consistent with the upper limit of 2000 kg derived from rare gas and radionuclide data by Bagolia et al. (1980). The initial mass of the Lost City meteoroid of 160 kg was derived consistently from both fireball dynamics and radiation by Ceplecha (1996) and confirmed by ReVelle and Ceplecha (2002). Similarly, the initial mass of Innisfree of 20–40 kg quoted by Halliday et al. (1981) is a consistent value. The luminous efficiency of Lost City and Innisfree was about 5%, somewhat less for these slower and smaller meteoroids than for Morávka. No photometry exists for Peekskill. The fireball was not registered by satellites, and visual data suggest that the peak brightness could be about −16 magnitude. Ceplecha at al. (1996) concluded from fireball dynamics that the initial mass was at least 10^4 kg. Graf et al. (1997), on the other hand, set a strong upper limit of 70 cm on the radius from radionuclide data, corresponding to 5000 kg. If we estimate that Peekskill was 10 times fainter on average than Morávka but lasted 5 times longer and that the luminous efficiency of Peekskill was half that of Morávka, we find that the initial kinetic energy of both meteoroids was of the same order. This will give

Fig. 17. The fall area landscape. View from Polomka (18.56° E, 49.51° N) to the north. The fall area extends beyond the horizon, which is ~12 km distant.

Table 5. Geophysical data on 6 meteorite falls (see Borovička et al. [2003a] for orbital data).

	Pribram	Lost City	Innisfree	Peekskill	Morávka	Neuschwanstein
Initial velocity (km/s)	20.9	14.1	14.5	14.7	22.5	20.9
Initial mass (kg)	1300[a]	160	30	5000[a]	1500	300
Trajectory slope to the horizontal	43°	38°	68°	3°	20°	49°
Beginning height (km)	98	86	≥62[b]	60[c]	80[c]	85
Peak absolute magnitude	−19	−12	−12	−16[c]	−20	−17
Duration of the fireball (s)	6.8	9.0	≥3.8[b]	≥30[c]	9[c]	5.3
Maximal dynamic pressure (MPa)	–	2.6	3.7	1.0	5.0	11.0
Terminal height (km)	13[c]	19	20	34 (30)[d]	21	16
Estimated total terminal mass (kg)	80	25	5	–	100	20
Estimated number of meteorites	≥17	≥5	≥9	–	>100	–
Number of recovered meteorites	4 (5)[e]	4	9	1	6	2[f]
Total recovered mass (kg)	5.8 (7)[e]	17	4.6	12.4	1.40	3.38[f]
References	Ceplecha (1961)	McCrosky et al. (1971), Ceplecha (1996)	Halliday et al. (1978, 1981)	Brown et al. (1994), Ceplecha et al. (1996)	This study	Spurný et al. (2003, 2002)

[a]Re-evaluated in this paper.
[b]Fireball beginning was captured only on low quality photo from large distance.
[c]Taking visual data into account.
[d]Theoretical extrapolation.
[e]Including 1 lost meteorite.
[f]DLR Press Information from July 29, 2003.

Peekskill a mass of 3500 kg. The 5000 kg given in Table 5 is an acceptable compromise. Data for Neuschwanstein were taken from the recent paper of Spurný et al. (2003), except for the dynamic pressure, which was computed from the values given in Spurný et al. (2002) and was confirmed by Spurný (personal communication).

In principal, the characteristics of a fireball and meteorite fall will depend on the initial velocity, mass, and slope of the trajectory in the atmosphere and the properties of the meteoroid. Table 5 contains 6 actual well-observed cases. Five are ordinary chondrites, while Neuschwanstein is an enstatite chondrite. Two are relatively small and slow meteoroids, Lost City and Innisfree. They produced fireballs of nearly full-moon brightness. About 85% of the initial mass was ablated during the atmospheric passage. Pribram and Morávka were more massive and substantially faster bodies that produced much brighter fireballs (superbolides, in fact). Due to larger velocity, the portion of ablated mass was larger, and reached about 94%. The same is true for a less massive but similarly fast Neuschwanstein. Peekskill was a large body with slow velocity. The nearly horizontal trajectory, however, is a peculiar aspect. An estimate of the total fallen mass was never made. A detailed analysis of fragments seen on video would be needed. Possibly, many meteorites have been spread over an extremely large area.

Maximal dynamic pressure acting on the meteoroids during the atmospheric flight was also computed (except for Pribram where the velocity could not been measured along the whole trajectory). The 5 MPa for Morávka is the second largest value, but Innisfree and Lost City suffered pressures of

similar magnitude. Neuschwanstein was exceptionally strong. The pressure was low for Peekskill, but this was a consequence of the shallow trajectory. The body was decelerated earlier than the time at which it reached dense atmospheric layers. The terminal heights of fireballs are lower in the case of steeper trajectories if the initial mass and velocity are comparable.

CONCLUSIONS

We presented a detailed analysis of the atmospheric fragmentation of the Morávka meteoroid based on video and seismic data. Such a study had never been done before, mainly because classical long exposure meteor photographs do not contain enough information because of overlapping fragment trails. Here, we were able to measure the relative positions of a number of individual fragments at individual time instants and relate them to the position of the main body, which was absolutely calibrated in terms of the trajectory and velocity.

In summary, the events connected to the Morávka meteorite fall are briefly descibed as follows: On May 6, 2000, 11:51:46 UT, a meteoroid of mass of about 1500 kg and size slightly less than 1 m entered the earth's atmosphere above southern Poland. The meteoroid's velocity relative to Earth was 22.5 km/s at the time of entry. The fireball was nearly heading south (toward azimuth 175.5°) with a horizontal slope of 20.4°. At a height of about 80 km above the ground, the ablation and evaporation was sufficiently intense that the fireball became visible to the naked eye in

broad daylight. The meteoroid was likely heavily prefractured from previous collisions in interplanetary space, as evidenced by the fact that it soon disintegrated into ~10 pieces with masses ranging from 100–200 kg. The height of this first fragmentation is uncertain, but it was >46 km. The primary fragments continued their flight close each to other, so the fireball appeared to be a single body with wake. Nevertheless, the atmospheric deceleration was measurably larger than would have corresponded to a single large body.

At heights of 37–29 km, all primary fragments broke-up again under dynamic pressures approaching 5 MPa. At this stage, the fireball reached its maximum luminosity, peaking at −20 absolute magnitude. The fragmentation cascade continued even though smaller pieces forming as part of the break-up process were increasingly decelerated and the dynamic pressure acting on them decreased. At each fragmentation, a significant portion of the mass of the parent fragment was lost in the form of dust or tiny particles. This was the dominant process of mass loss. The continuous ablation due to melting and evaporation of the meteoroid surface was less efficient at removing mass. The corresponding ablation coefficient was less than 0.003 s^2 km^{-2}. Small luminous droplets, which we term "sparks," were observed for the first time in the wake of macroscopic fragments.

The fragmentation process led to a significant dispersion of the fragments. Some pieces achieved lateral velocities of up to 300 m/s, an order of magnitude more than can be explained by aerodynamic loading. After being decelerated below a velocity of 3–4 km/s, the radiation and ablation of the meteoroid fragments ceased, but in many cases, the fragmentation continued, as demonstrated by the incomplete fusion crust coverage of recovered meteorites. We estimate that several hundreds of meteorites with a total mass of ~100 kg landed. They are spread in a strewn field ~20 km long, extending both to the north and to the south of the village of Morávka in the Czech Republic. The mass of the largest meteorite might be about 8 kg, unless it fragmented further after the cessation of ablation at the height of ~20 km. Only 6 meteorites with a total mass 1.4 kg are known to have been recovered through the end of May 2003. This low recovery efficiency can be ascribed to the mountainous and forested terrain covering most of the fall area.

REFERENCES

Artemieva N. A. and Shuvalov V. V. 2001. Motion of a fragmented meteoroid through the planetary atmosphere. *Journal of Geophysical Research* 106:3297–3309.

Bagolia C., Bhandari N., Sinha N., Goswani J. N., Lal D., Lorin J. C., and Pellas P. 1980. Multiple fall of Pribram meteorites photographed. 12. Pre-atmospheric size of the Pribram meteorite based on studies of fossil cosmic ray tracks and spallation products. *Bulletin of the Astronomical Institutes of Czechoslovakia* 31:51–58.

Baldwin B. and Sheaffer Y. 1971. Ablation and breakup of large meteoroids during atmospheric entry. *Journal of Geophysical Research* 76:4653–4668.

Beech M., Brown P., Hawkes R. L., Ceplecha Z., Mossman K., and Wertherill G. 1995. The fall of the Peekskill meteorite: Video observations, atmospheric path, fragmentation record, and orbit. *Earth, Moon, and Planets* 68:189–197.

Borovička J., Popova O. P., Nemtchinov I. V., Spurný P., and Ceplecha Z. 1998. Bolides produced by impacts of large meteoroids into the earth's atmosphere: Comparison of theory and observations. I. Benesov bolide dynamics and fragmentation. *Astronomy and Astrophysics* 334:713–728.

Borovička J., Spurný P., Kalenda P., and Tagliaferri E. 2003a. The Morávka meteorite fall. 1. Description of the events and determination of the fireball trajectory and orbit from video records. *Meteoritics & Planetary Science.* This issue.

Borovička J., Weber H. W., Jopek T., Jakeš P., Randa Z., Brown P. G., ReVelle D. O., Kalenda P., Schultz L., Kucera J., Haloda J., Týcová P., Frýda J., and Brandstätter F. 2003b. The Morávka meteorite fall. 3. Meteoroid initial size, history, structure, and composition. *Meteoritics & Planetary Science.* This issue.

Bronshten V. A. 1983. *Physics of meteor phenomena.* Dordrecht: Reidel. 356 p.

Brown P., Ceplecha Z., Hawkes R. L., Wertherill G., Beech M., and Mossman K. 1994. The orbit and atmospheric trajectory of the Peekskill meteorite from video records. *Nature* 367:624–626.

Brown P. G., Kalenda P., ReVelle D. O., and Borovička J. 2003. The Morávka meteorite fall. 2. Interpretation of infrasonic and seismic data. *Meteoritics & Planetary Science.* This issue.

Ceplecha Z. 1961. Multiple fall of Pribram meteorites photographed. 1. Double-station photographs of the fireball and their relations to the found meteorites. *Bulletin of the Astronomical Institutes of Czechoslovakia* 12:21–47.

Ceplecha Z. 1996. Luminous efficiency based on photographic observations of the Lost City fireball and implications for the influx of interplanetary bodies onto Earth. *Astronomy and Astrophysics* 311:329–332.

Ceplecha Z., Spurný P., Borovička J., and Keclíková J. 1993. Atmospheric fragmentation of meteoroids. *Astronomy and Astrophysics* 279:615–626.

Ceplecha Z., Brown P., Hawkes R. L., Wertherill G., Beech M., and Mossman K. 1996. Video observations, atmospheric path, orbit, and fragmentation record of the fall of the Peekskill meteorite. *Earth, Moon, and Planets* 72:395–404.

Ceplecha Z., Borovička J., Elford W. G., ReVelle D. O., Hawkes R. L., Porubcan V., and Šimek M. 1998. Meteor phenomena and bodies. *Space Science Reviews* 84:327–471.

Docobo J. A. and Ceplecha Z. 1999. Video record (CD copy

attached) of the Spain bolide of June 14, 1996: The atmospheric trajectory and orbit. *Astronomy and Astrophysics Supplemental Series* 138:1–9.

Foschini L. 2001. On the atmospheric fragmentation of small asteroids. *Astronomy and Astrophysics* 365:612–621.

Graf T., Marti K., Xue S., Herzog G. F., Klein J., Middleton R., Metzler K., Herd R., Brown P., Wacker J. F., Jull A. J. T., Masarik J., Koslowsky V. T., Andrews H. R., Cornett R. J. J., Davies W. G., Greiner B. F., Imahori Y., Mckay J. W., Milton G. M., and Milton J. C. D. 1997. Exposure history of the Peekskill (H6) meteorite. *Meteoritics & Planetary Science* 32:25–30.

Halliday I., Griffin A. A., and Blackwell A. T. 1978. The Innisfree meteorite and the Canadian camera network. *Journal of the Royal Astronomical Society of Canada* 72:15–39.

Halliday I., Griffin A. A., and Blackwell A. T. 1981. The Innisfree meteorite fall: A photographic analysis of fragmentation, dynamics, and luminosity. *Meteoritics* 16:153–170.

Hills J. G. and Goda M. P. 1993. The fragmentation of small asteroids in the atmosphere. *The Astronomical Journal* 105:1114–1144.

Jenniskens P., Betlem H., Betlem J., Barifaijo E., Schluter T., Hampton C., Laubenstein M., Kunz J., and Heusser G. 1994. The Mbale meteorite shower. *Meteoritics* 29:246–254.

McCrosky R. E., Posen A., Schwartz G., and Shao C. Y. 1971. Lost City meteorite—Its recovery and a comparison with other fireballs. *Journal of Geophysical Research* 76:4090–4108.

ReVelle D. O. and Ceplecha Z. 2002. Semi-empirical fragmentation model of meteoroid motion and radiation during atmospheric penetration. In *Asteroids, comets, meteors 2002,* edited by Warmbein B. ESA Special Publication #500. pp. 285–288.

Spurný P., Heinlein D., and Oberst J. 2002. The atmospheric trajectory and heliocentric orbit of the Neuschwanstein meteorite fall on April 6, 2002. In *Asteroids, Comets, Meteors 2002,* edited by Warmbein B. ESA Special Publication #500. pp. 137–140.

Spurný P., Oberst J., and Heinlein D. 2003. Photographic observations of Neuschwanstein, a second meteorite from the orbit of the Pribram chondrite. *Nature* 423:151–153.

Stulov V. P. and Titova L. Yu. 2001. Comparative analysis of models for disintegration of meteoric bodies. *Solar System Research* 35: 315–319.